Electronic Supplementary Material (ESI) for Physical Chemistry Chemical Physics.

Supplementary Information

Effects of substituent position on aminobenzoate relaxation pathways in solution

Natércia d. N. Rodrigues,*[a,b] Jack M. Woolley,[a] Konstantina M. Krokidi,[a] Maria A. Tesa-Serrate,[c] Matthew A. P. Turner,[a,d] Nicholas D. M. Hine[d] and Vasilios G. Stavros*[a]

[a] *University of Warwick, Department of Chemistry, Coventry, CV4 7AL, UK*
[b] *Lipotec SAU, Calle Isaac Peral, 17 Pol. Ind. Camí Ral, 08850 Barcelona, Spain*
[c] *Edinburgh Instruments, 2 Bain Square, Kirkton Campus, Livingston, EH54 7DQ, UK*
[d] *University of Warwick, Department of Physics, Coventry, CV4 7AL, UK*

*Corresponding author's e-mail: natercia.rodrigueslopes@lubrizol.com, v.stavros@warwick.ac.uk

S1. Temperature-dependent Absorption Spectra

Temperature-dependent Ultraviolet/Visible (UV/Vis) absorption spectra of both *m*-MA (methyl-3-aminobenzoate, Alfa Aesar, ≥98%) and *p*-MA (methyl-4-aminobenzoate, Aldrich, 98%) dissolved in cyclohexane (CHX, Merck, ≥99.7%), acetonitrile (ACN, Fisher Scientific, ≥99.8%), and ethanol (EtOH, VWR, absolute) were obtained with an Agilent Cary 60 UV/Vis spectrophotometer equipped with a temperature control unit (TC 1 Temperature Controller, Quantum NorthWest). The absorption spectra for each solution were taken first at 15°C and then in increasing 10°C steps up to 75°C, allowing 30 minutes in between each scan for temperature equilibration. The spectra obtained following this procedure are shown in Figure S1 for *m*-MA, and Figure S2 for *p*-MA.

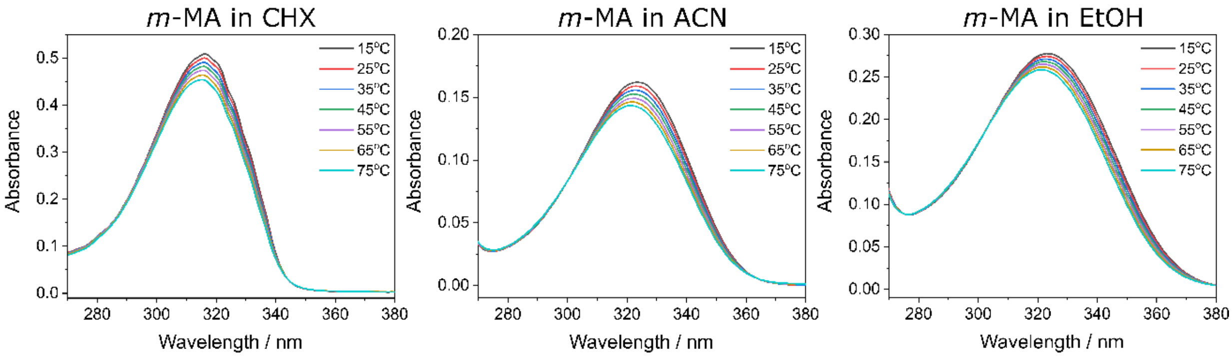

Figure S1: Temperature-dependent UV/Vis spectra for *m*-MA in (left) CHX, (middle) ACN, and (right) EtOH. Each spectrum was acquired after 30 minutes to allow for temperature equilibration.

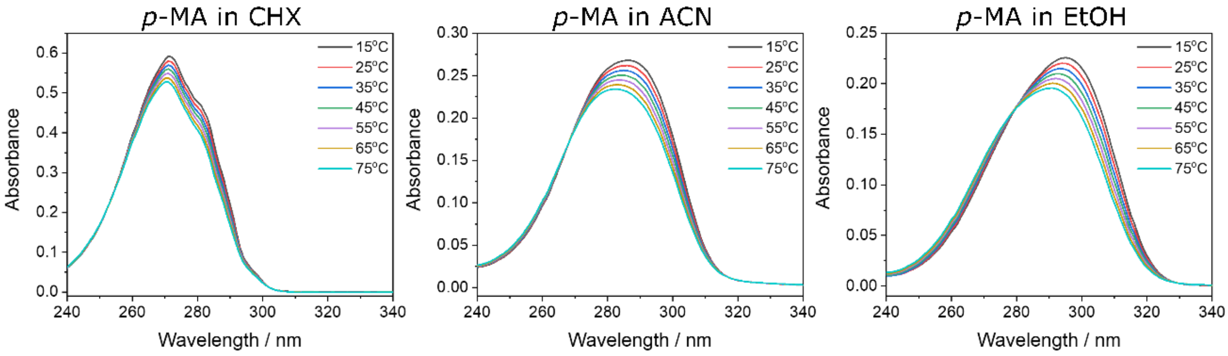

Figure S2: Temperature-dependent UV/Vis spectra for *p*-MA in (left) CHX, (middle) ACN, and (right) EtOH. Each spectrum was acquired after 30 minutes to allow for temperature equilibration.

S2. Fluorescence Quantum Yields

The methodology followed for the determination of fluorescence quantum yields has been described in detail by Würth *et al.*,[1] by comparing the emission intensity of the samples of interest (denoted x below) with those of known standards (denoted s below). Briefly, all sample and standard solutions, detailed in Table S1, were prepared at 10^{-3} M concentration and were further diluted in a 1 cm pathlength quartz cuvette as required to achieve an absorbance of ~0.1 at the wavelength of interest (comparable to the pump wavelength, λ_{pu}, used in ultrafast experiments, see main manuscript). Five scans of the emission spectra were taken for each solution using a Horiba Scientific Fluorolog®-3 spectrofluorometer with a slit width of 5 mm. The average of these five scans for each sample was used to calculate the respective fluorescence quantum yields (Φ_{Fl}) using the following equation:

$$\Phi_{\mathrm{Fl}}^{x} = \frac{\mathrm{F}_x f_s n_x^2}{\mathrm{F}_s f_x n_s^2} \Phi_{\mathrm{Fl}}^{s}$$

where F_x and F_s refer to integral photon flux, taken here to be the area under the emission curves of each sample and standard, respectively. In addition, $f = 1 - 10^{-A}$, where A is the absorbance at the wavelength of interest, and n is the refractive index of the solvent for each solution at the wavelength of interest. The calculated values of Φ_{Fl} following this method are presented in Table S1.

Table S1: List of sample and standard solutions used to measure the fluorescence quantum yield (Φ_{Fl}) of *m*- and *p*-MA. All solutions were initially prepared to a concentration of 10^{-3} M and further diluted as needed to achieved an absorbance of ~0.1. The values for each molecule in CHX are displayed here as previously reported.[2]

Molecule	Solvent	Standard	Φ_{Fl}
m-MA	CHX	DPB in CHX	0.25[2]
	ACN	1,4-diphenyl-1,3-butadiene in CHX	0.78 ± 0.02
	EtOH	1,4-diphenyl-1,3-butadiene in CHX	0.64 ± 0.02
p-MA	CHX	DPB in CHX	0.08[2]
	ACN	3,3’5,5-tetramethylbenzidine in EtOH	0.45 ± 0.001
	EtOH	3,3’5,5-tetramethylbenzidine in EtOH	0.15 ± 0.07

S3. Fluorescence Lifetimes

The fluorescence lifetimes (τ_{Fl}) of *m*-MA were measured in a 1 cm pathlength quartz cuvette for ~0.01 mM solutions of *m*-MA dissolved in ACN and EtOH; the corresponding measurement for *m*-MA in CHX, following similar methodology, has previously been reported ($\tau_{\mathrm{Fl}} \sim 1.7$ ns).[2] The time-resolved emission spectra were recorded with a Horiba Fluorolog®-3 spectrofluorometer employing a 318 nm NanoLED as the photoexcitation light source. Blank traces were also collected in order to determine the instrument response associated with these measurements. The fluorescence lifetime values were extracted by fitting the time-resolved emission traces with an exponential decay convolved with a Gaussian function to account for the instrument response. The results, shown in Figure S3, yield fluorescence lifetimes of $\tau_{\mathrm{Fl}} = 10.24 \pm 0.02$ ns for *m*-MA in ACN, and $\tau_{\mathrm{Fl}} = 14.00 \pm 0.03$ ns for *m*-MA in EtOH; the quoted errors are the errors associated with the fit.

For *p*-MA, the fluorescence lifetimes were measured by Time-Correlated Single Photon Counting (TCSPC) in a FS5 Spectrofluorometer (Edinburgh Instruments Ltd.) equipped with a standard cuvette holder, TCSPC electronics, and an EPLED-280 diode laser for excitation. The instrument response function was measured by placing a scattering solution (Ludox) in the sample position and tuning the emission wavelength to that of the excitation source. All TCSPC fluorescence lifetime measurements for *p*-MA were obtained with photoexcitation at 279 nm and by monitoring emission at 340 nm, with a slit width ($\Delta\lambda_{\mathrm{em}}$) of 7 nm, time resolution of 24 ps/channel, and 2 MHz repetition rate. The resulting emission decay curves, shown in Figures S4 to S6, were fitted with a multiexponential decay model using the reconvolution algorithm included in the Fluoracle software that accompanies the FS5 Spectrofluorometer. Employing this method, the fluorescence lifetimes of *p*-MA were determined to be $\tau_{\mathrm{Fl}} = 1.949 \pm 0.003$ ns in CHX, $\tau_{\mathrm{Fl}} = 1.029 \pm 0.002$ ns in ACN, and $\tau_{\mathrm{Fl}} = 0.4 \pm 0.1$ ns in EtOH (see main manuscript for further discussion); the quoted errors are the errors associated with the fit.

Finally, we note here that the justification for employing different techniques to measure the fluorescence lifetimes of *m*- and *p*-MA is merely logistic: the Horiba Scientific Fluorolog®-3 employed in these experiments was not fitted with the appropriate light source to photoexcite *p*-MA and, on the other hand, the available TCSPC experiments were not equipped to photoexcite *m*-MA.

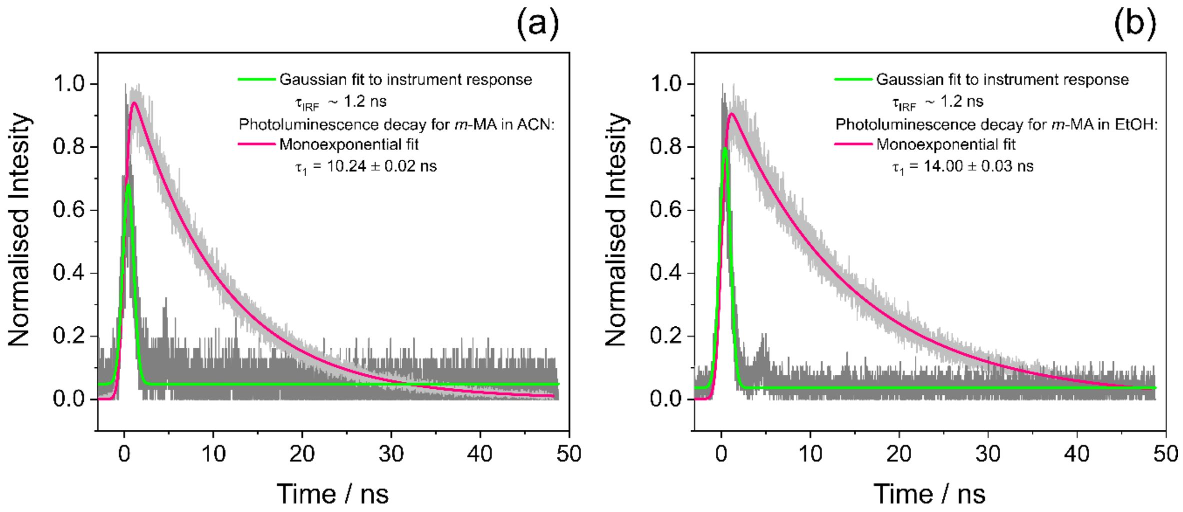

Figure S3: Fluorescence lifetime traces for *m*-MA in (a) ACN and (b) EtOH, both obtained with the Horiba Scientific Fluorolog®-3 spectrofluorometer. In both graphs, the raw traces for the instrument response (dark grey) and the measurements (light grey) are shown alongside the corresponding fits (green lines for instrument response and pink lines for the fluorescence lifetime fit).

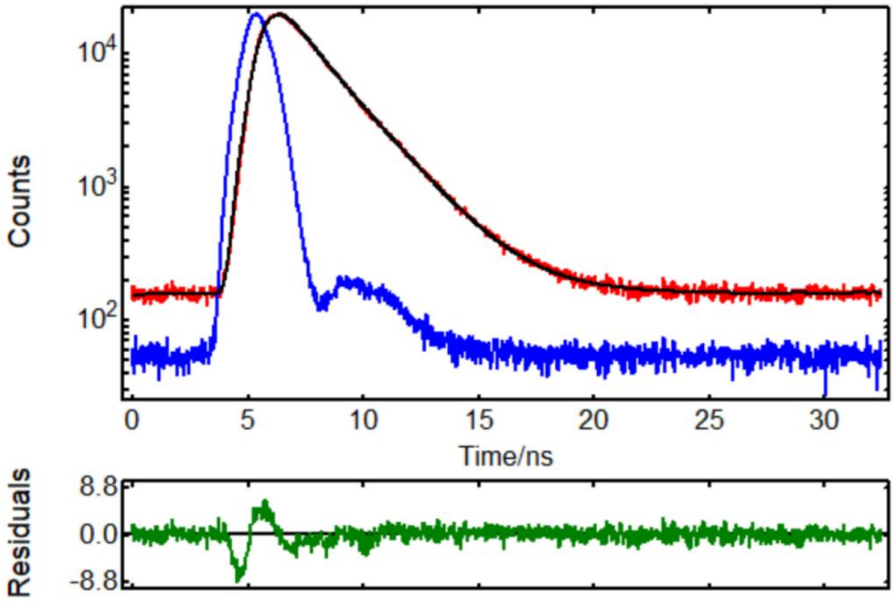

Figure S4: TCSPC decay of *p*-MA in cyclohexane: experimental decay (red), IRF (blue), fit result (black), and residuals (green). These measurements were obtained for photoexcitation with 279 nm and by monitoring emission at 340 nm ($\Delta\lambda_{em}$ = 7 nm). The time resolution of these measurements is 24 ps/channel, and they were ran at 2 MHz repetition rate.

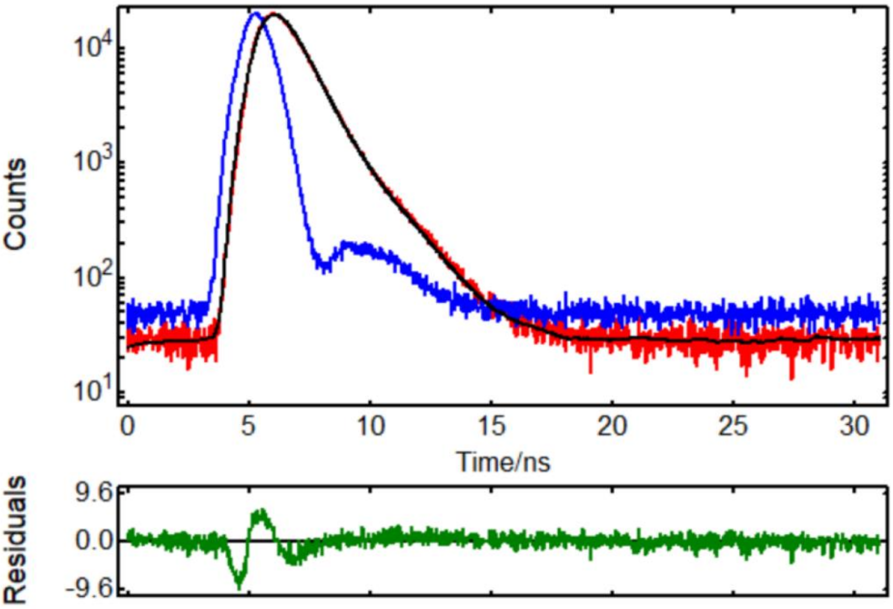

Figure S5: TCSPC decay of *p*-MA in acetonitrile: experimental decay (red), IRF (blue), fit result (black), and residuals (green). These measurements were obtained for photoexcitation with 279 nm and by monitoring emission at 340 nm ($\Delta\lambda_{em}$ = 7 nm). The time resolution of these measurements is 24 ps/channel, and they were ran at 2 MHz repetition rate.

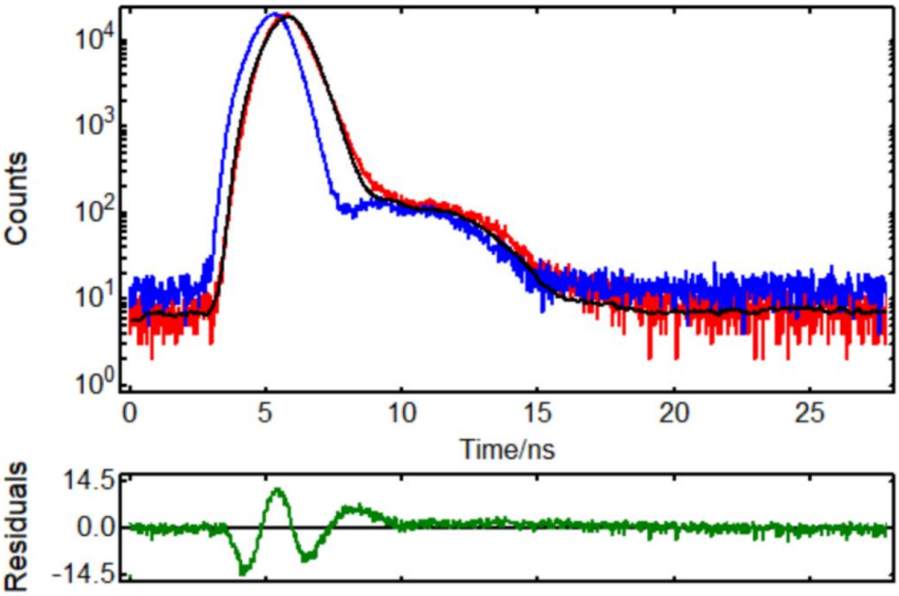

Figure S6: TCSPC decay of *p*-MA in ethanol: experimental decay (red), IRF (blue), fit result (black), and residuals (green). These measurements were obtained for photoexcitation with 279 nm and by monitoring emission at 340 nm ($\Delta\lambda_{em}$ = 7 nm). The time resolution of these measurements is 24 ps/channel, and they were ran at 2 MHz repetition rate.

S4. Power Dependence Studies

Under laser irradiation conditions, multiphoton absorption is possible, and this may initiate photodynamics that are not possible under solar irradiation, for which photodynamics are almost completely induced by single-photon absorption (multiphoton effects under solar irradiation are negligible). Hence, multiphoton-induced photodynamics are outside of the scope of our work, which aims to explore the photodynamics of sunscreen UV filters. To ensure single-photon initiated photodynamics, power dependence studies are carried out for each sample studied. These studies consist of collecting TEAS data at a selected number of time delays (Δt) and at different pump laser powers. The logarithm of transient signal with respect to the logarithmic value of power for each time delay (log(signal) vs. log(power)) is then plotted and the resulting data is fitted using a linear function using least squares regression. The gradient of this fit provides physical information regarding the signal-power dependence, *i.e.* a gradient of 1 (within error) is taken to be indicative of single-photon dynamics. Figures S7 and S8 show a representative sample of such plots, which lead us to confidently conclude that the presented photodynamics result from single-photon absorption and are, therefore, relevant to the purpose of understanding the ultrafast photodynamics of *m*-MA and *p*-MA in the context of sunscreen use.

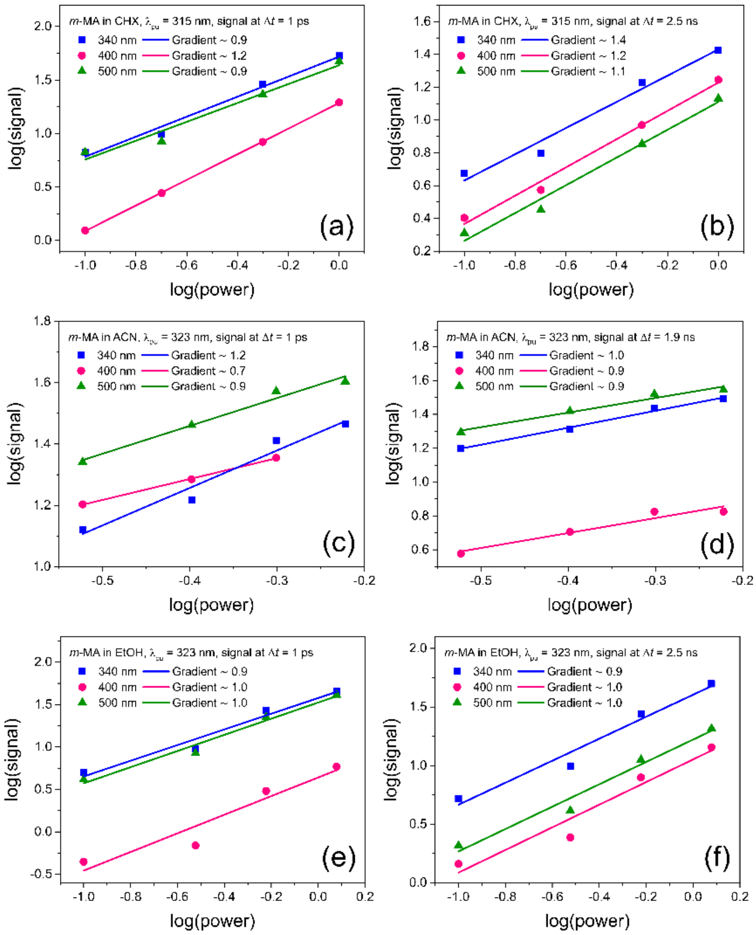

Figure S7: Power dependence studies for samples of *m*-MA in (a) CHX at Δt = 1 ps, (b) CHX at Δt = 2.5 ns, (c) ACN at Δt = 1 ps, (d) ACN at Δt = 1.9 ns, (e) EtOH at Δt = 1 ps, and (f) EtOH at Δt = 2.5 ns. These power dependence studies were repeated, for each solvent and at each time delay, for different wavelengths in order to sample the signal across the probe wavelength window of these experiments.

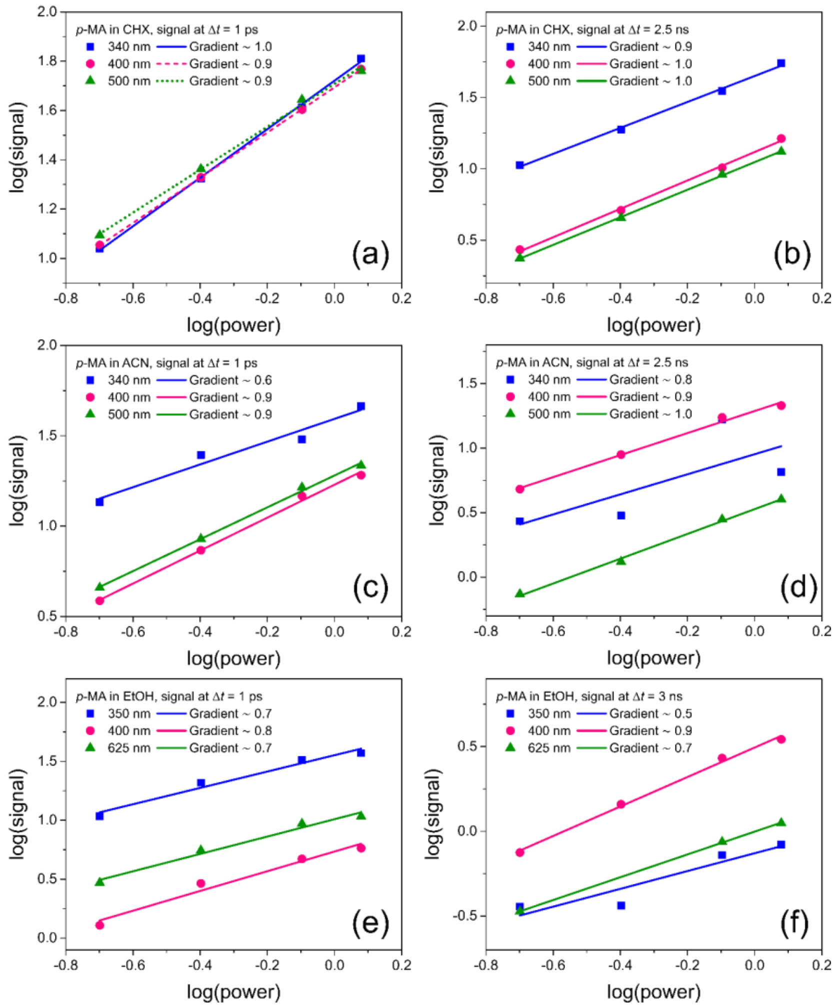

Figure S8: Power dependence studies for samples of *p*-MA in (a) CHX at Δ*t* = 1 ps, (b) CHX at Δ*t* = 2.5 ns, (c) ACN at Δ*t* = 1 ps, (d) ACN at Δ*t* = 2.5 ns, (e) EtOH at Δ*t* = 1 ps, and (f) EtOH at Δ*t* = 3 ns. These power dependence studies were repeated, for each solvent and at each time delay, for different wavelengths in order to sample the signal across the probe wavelength window of these experiments.

S5. Fitting procedure

The transient electronic absorption spectroscopy (TEAS) data collected was globally fit using the Glotaran software package.[3] The algorithm employed includes several components to account for different experimental measurables. Firstly, the TEAS data obtained in the presented work and presented in the main manuscript is inherently chirped, *i.e.* Δ*t* = 0 is different for each probe wavelength (λ_{pr}), due to group velocity dispersion (GVD) artefacts,[4] which is accounted for by including a third order polynomial in the fitting algorithm.[3] This chirp effect was corrected in the TAS presented in Figures 4 and 7 in the main manuscript using the KOALA package.[5] Moreover, assuming here a sequential kinetic model (A $\xrightarrow{\tau_1}$ B $\xrightarrow{\tau_2}$ C, as is the assumption throughout the main manuscript) the global fitting algorithm in Glotaran models the data for each λ_{pr} and each Δ*t* with a superposition Ψ of *n* components l:

$$\Psi(\lambda_{\mathrm{pr}}, \Delta t) = \sum_{l=1}^{n} c_l^{\mathrm{EADS}}(\Delta t, \theta)\,\mathrm{EADS}_l(\lambda_{\mathrm{pr}})$$

In the equation above, c_l^{EADS} is a linear combination of exponential decays convolved with the Gaussian instrument response function (IRF, approximately 70-140 fs, see below) and EADS_l is the evolution associated difference spectra associated with component l. For each set of initial parameters θ, the model is iterated until convergence is achieved and the quality of the fit is evaluated by analysis of the resulting residuals, which correspond to the difference between the fit and the raw data at each data point. This fitting procedure allows us to extract quantitative dynamical information by yielding time constants, τ, associated with each evolution associated difference spectra (EADS). These are the time constants reported in Table 2 of the main manuscript.

S6. Instrument Response Function

The temporal cross-section of our pump and probe laser pulses, as well as any potential solvent-only photodynamics, determine the fastest time constant (τ) that can be extracted from our experiments. The combination of these quantities is encompassed in the instrument response function (IRF). The IRF for our TEAS experiments is determined by collecting solvent-only responses and fitting them with a Gaussian function of the form

$$Fit = y_0 + \sum_n \left(\frac{A_n}{w_n \times \sqrt{\pi/2}} \right) \times e^{-2\times\left(x-c_n/w_n\right)^2}$$

where y_0 is a signal baseline offset, A_n and c_n are the intensity and the centre of the Gaussian curve, respectively, and w_n is the width of the Gaussian function. The width, w_n, of the most intense Gaussian curve required to fit the data is taken to be the IRF at the experimental conditions corresponding to the given solvent-response data; Figure S9 shows a number of such plots for a number of combinations of solvent, pump wavelengths (those used for the TEAS experiments reported on in the main manuscript) and probe wavelengths. Due to varying group velocity mismatch between the pump and the spectral components of the probe,[6,7] the IRF is probe dependent. Hence, we take the worst-case scenario and do not quote any lifetimes that are shortest than the widest IRF found which is, in the case of these experiments, approximately 140 fs.

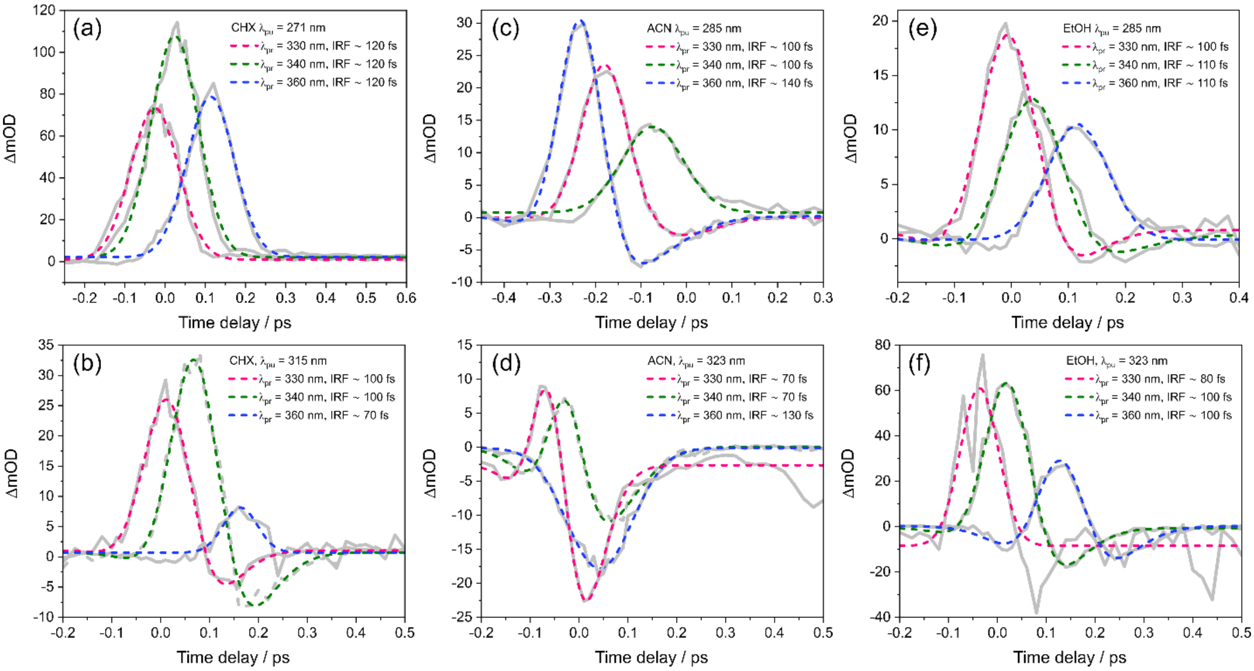

Figure S9: Example instrument response functions (IRF) for the TEAS setup described in the main paper, for the solvent and λ_{pu} combinations used in the presented TEAS experiments: (a) CHX at 271 nm, (b) CHX at 315 nm, (c) ACN at 285 nm, (d) ACN at 323 nm, (e) EtOH at 285 nm, and (f) EtOH at 323 nm. Raw data are shown as grey solid lines; gaussian fits are show in pink, green and blue for λ_{pr} = 330, 340, and 360 nm, respectively. Note: (a) and (e) were obtained for a 100 µm sample path length, while all others were obtained for 500 µm sample path length.

S7. Fit Residuals

As mentioned in section S5, the quality of the fits obtained from global fitting with Glotaran is evaluated from analysis of the residuals produced as a result of the fitting procedure. These residuals correspond to the difference between the value of the fit and the value of the raw data for each data point, hence the perfect fit would yield a value of zero across all data points. Figures S10 and S11 show the residuals obtained from fitting the data presented in the main manuscript following the procedure detailed in S5. In addition, it is useful to evaluate the quality of the fit for specific probe wavelengths; these lineouts are shown in Figures S12 and S13.

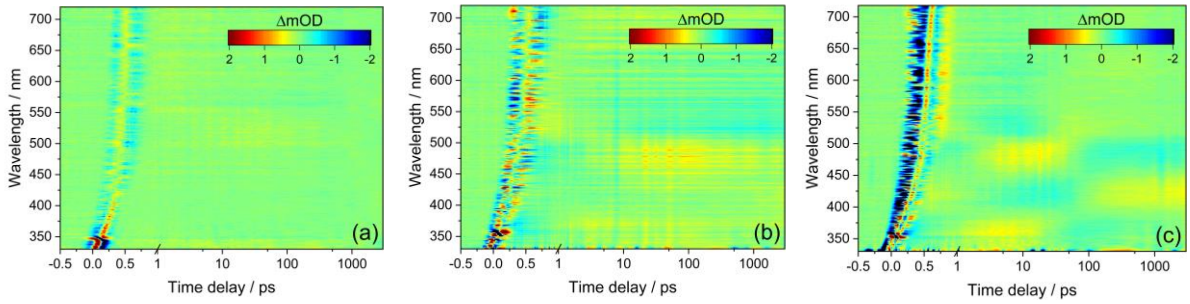

Figure S10: Residuals resulting from the aforementioned global fitting of the TEAS data collected for *m*-MA in (a) CHX, (b) ACN and (c) EtOH.

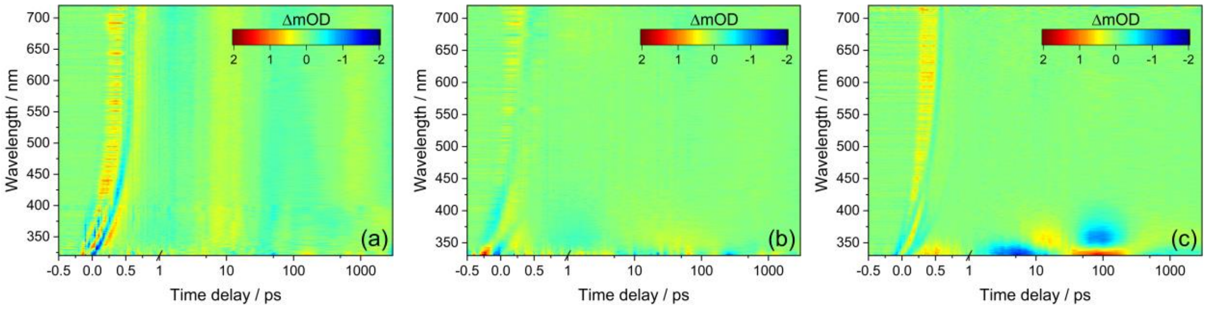

Figure S11: Residuals resulting from the aforementioned global fitting of the TEAS data collected for *p*-MA in (a) CHX, (b) ACN and (c) EtOH.

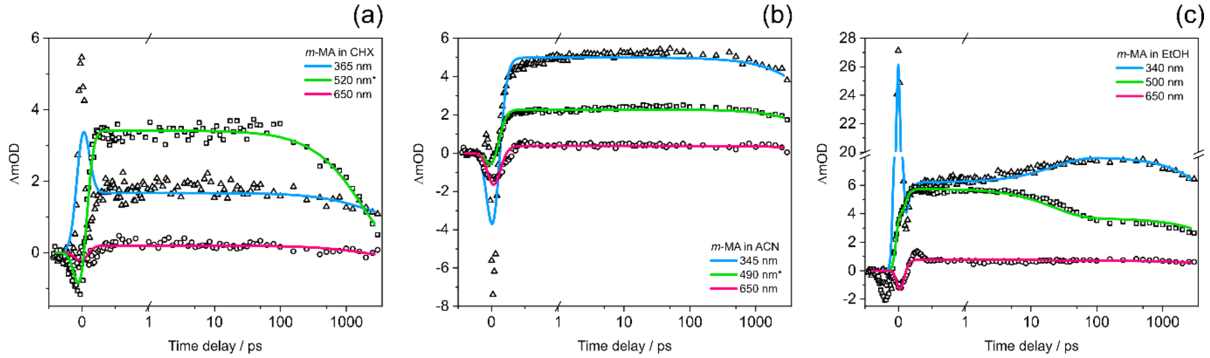

Figure S12: Transient data (symbols) and respective fits (solid lines), as obtained from global fitting, at specific wavelengths for *m*-MA in (a) CHX, (b) ACN, and (c) EtOH. The traces marked with * were scaled for clarity. Specifically, in the CHX traces (a), the 520 nm trace and fit were multiplied by 2, while in the ACN traces (b) the 490 nm trace and fit were divided by 2.

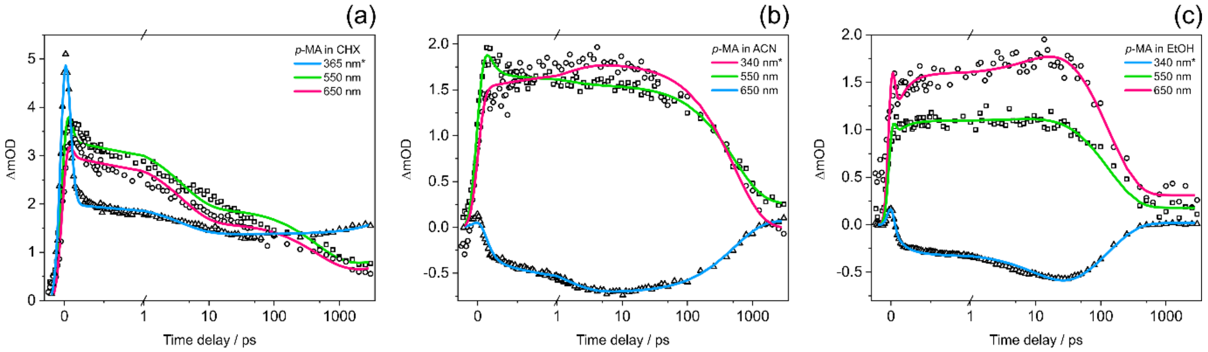

Figure S13: Transient data (symbols) and respective fits (solid lines), as obtained from global fitting, at specific wavelengths for *p*-MA in (a) CHX, (b) ACN, and (c) EtOH. The traces marked with * were scaled for clarity. Specifically, in the CHX traces (a), the 365 nm trace and fit were divided by 3; in the ACN traces (b) the 340 nm trace and fit were divided by 10; and in the EtOH traces (c) the 340 nm trace and fit were divided by 20.

S8. Supplementary Computational Results

In an attempt to locate a charge-transfer (CT) energy minimum that would justify the large, solvent-dependent Stokes shifts observed for *m*-MA (see main manuscript), we probed two reaction coordinates for this molecule in implicitly modelled ethanol, the solvent for which the largest Stokes shift is observed. The most obvious molecular motions that could lead to a CT energy minimum away from the Franck-Condon region in *m*-MA are the rotations of the amino group, akin to what was suggested and modelled for *p*-MA (see main manuscript), or of the ester group. As also detailed in the Computational Methods section in the main manuscript, these reaction coordinates of interest were probed in implicit ethanol along the static rotation of the bond through equidistant steps along the coordinate with vertical excitations calculated at every step at the PBE0/cc-pVTZ level of theory.

The results of the computational procedure just described reveal that there is a significant barrier to the rotation of the amino group of *m*-MA in its S_1 state, as shown in Figure S14. This observation confirms that, like *p*-MA, *m*-MA is not a twist intramolecular charge transfer (TICT) system (see main manuscript for further discussion). In addition, the aforementioned computational procedure also revealed a significant barrier to the rotation of the ester substituent group of *m*-MA, as shown in Figure S15. For completeness, the equivalent rotation of the ester group in *p*-MA was also performed, with the results being shown in Figure S16.

As such, we were unable to find a CT energy minimum that may justify the experimental observations in *m*-MA following these two most obvious reaction coordinates, in particular the large, solvent-dependent Stokes shifts reported on in the main manuscript. Our excited state geometry relaxation calculations also optimized to what is likely a local minimum in the vicinity of the Franck-Condon region, and as such provide no evidence for a lower energy CT energy minimum that could account for our experimental observations. While a full search of the S_1 surface of *m*-MA in implicitly modelled solvent could potentially locate this CT minimum, this demanding computational study is beyond the scope of this work, and it is nevertheless likely that explicit solvent models may be required to appropriately model the spectroscopic behaviour of both *m*-MA and *p*-MA.

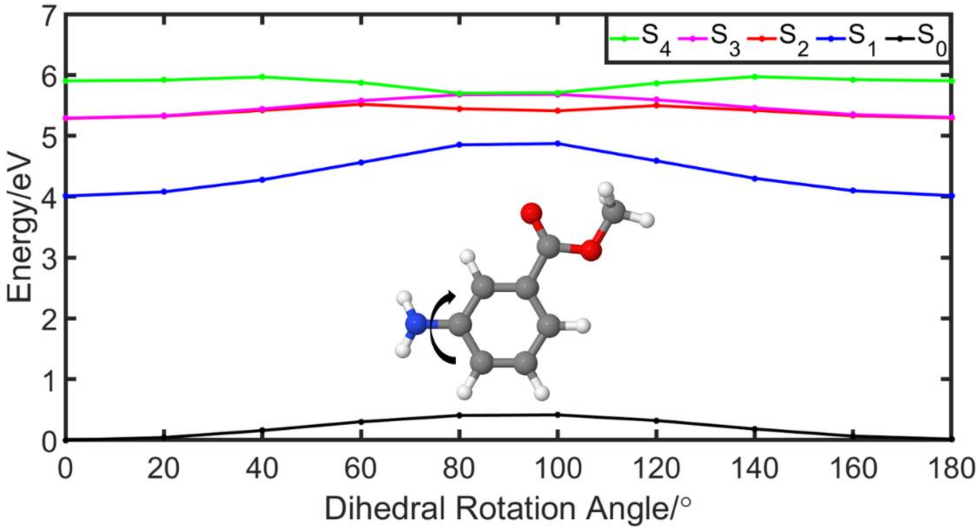

Figure S14: A plot of the calculated energies of the ground (S_0, black) and first four excited states of *m*-MA: S_1 (blue), S_2 (red), S_3 (pink), and S_4 (green). The arrows illustrate the dihedral angle that has been rotated in order to probe for local minima, *i.e.* the rotation of the amino group (NH_2). The origin, at 0 degrees, denotes the Franck-Condon region, with each subsequent angle being the rotation along the respective dihedral angle. These potential energy curves were produced at the PBE0/cc-pVTZ level of theory, and all calculations were conducted using implicitly modelled ethanol.

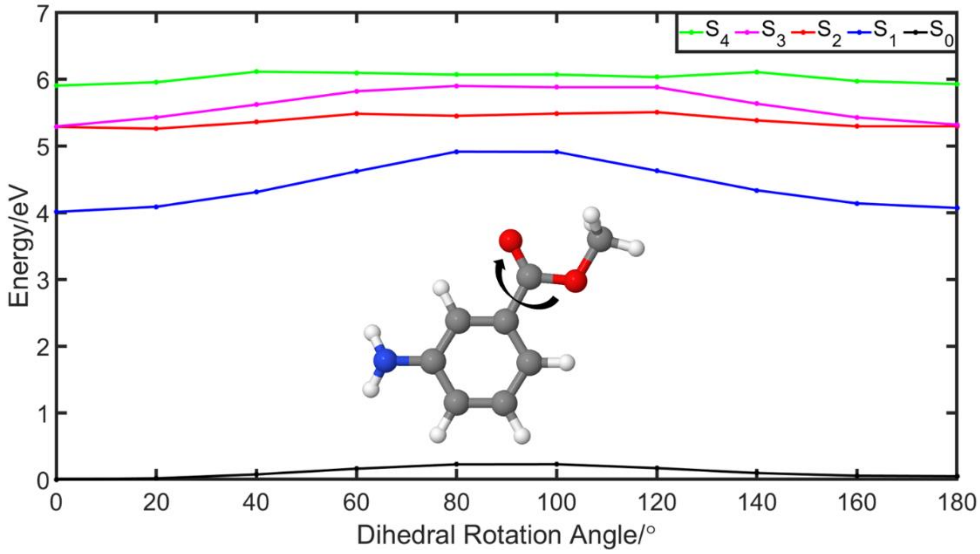

Figure S15: A plot of the calculated energies of the ground (S_0, black) and first four excited states of *m*-MA: S_1 (blue), S_2 (red), S_3 (pink), and S_4 (green). The arrows illustrate the dihedral angle that has been rotated in order to probe for local minima, *i.e.* the rotation of the ester group. The origin, at 0 degrees, denotes the Franck-Condon region, with each subsequent angle being the rotation along the respective dihedral angle. These potential energy curves were produced at the PBE0/cc-pVTZ level of theory, and all calculations were conducted using implicitly modelled ethanol.

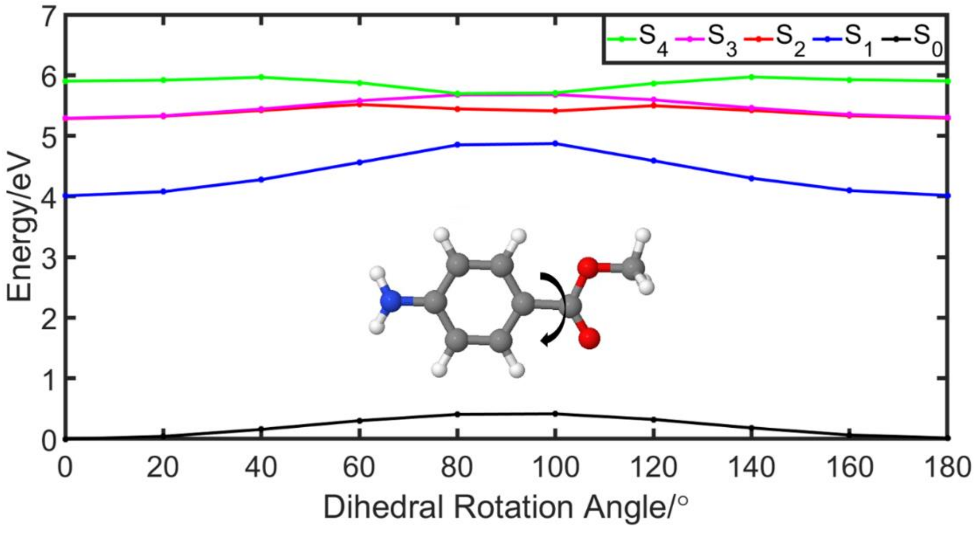

Figure S16: A plot of the calculated energies of the ground (S_0, black) and first four excited states of *p*-MA: S_1 (blue), S_2 (red), S_3 (pink), and S_4 (green). The arrows illustrate the dihedral angle that has been rotated in order to probe for local minima, i.e. the rotation of the ester group. The origin, at 0 degrees, denotes the Franck-Condon region, with each subsequent angle being the rotation along the respective dihedral angle. These potential energy curves were produced at the PBE0/cc-pVTZ level of theory, and all calculations were conducted using implicitly modelled ethanol.

References

1 C. Würth, M. Grabolle, J. Pauli, M. Spieles and U. Resch-Genger, Relative and absolute determination of fluorescence quantum yields of transparent samples, *Nat. Protoc.*, 2013, **8**, 1535–1550.

2 N. d. N. Rodrigues, N. C. Cole-Filipiak, M. A. P. Turner, K. Krokidi, G. L. Thornton, G. W. Richings, N. D. M. Hine and V. G. Stavros, Substituent position effects on sunscreen photodynamics: A closer look at methyl anthranilate, *Chem. Phys.*, 2018, **515**, 596–602.

3 J. J. Snellenburg, S. P. Laptenok, R. Seger, K. M. Mullen and I. H. M. van Stokkum, Glotaran : A Java -Based Graphical User Interface for the R Package TIMP, *J. Stat. Softw.*, , DOI:10.18637/jss.v049.i03.

4 I. Walmsley, L. Waxer and C. Dorrer, The role of dispersion in ultrafast optics, *Rev. Sci. Instrum.*, 2001, **72**, 1–29.

5 M. P. Grubb, A. J. Orr-Ewing and M. N. R. Ashfold, KOALA: A program for the processing and decomposition of transient spectra, *Rev. Sci. Instrum.*, 2014, **85**, 064104.

6 U. Megerle, I. Pugliesi, C. Schriever, C. F. Sailer and E. Riedle, Sub-50 fs broadband absorption spectroscopy with tunable excitation: putting the analysis of ultrafast molecular dynamics on solid ground, *Appl. Phys. B*, 2009, **96**, 215–231.

7 I. Z. Kozma, P. Krok and E. Riedle, Direct measurement of the group-velocity mismatch and derivation of the refractive-index dispersion for a variety of solvents in the ultraviolet, *J. Opt. Soc. Am. B*, 2005, **22**, 1479.